PAPER

Ideal and resistive impurity parallel-velocity-gradient instability

IOP Publishing Plasma Physics and Controlled Fusion
Plasma Phys. Control. Fusion **67** (2025) 075019 (17pp) https://doi.org/10.1088/1361-6587/ade4fb

Ideal and resistive impurity parallel-velocity-gradient instability

G Cuerva-Lazaro[1,2,*], M Lesur[1,3], O D Gürcan[4], J Bourgeois[5,6,7], C Maestracci[1], E Gravier[1] and Y Kosuga[8,9]

[1] Université de Lorraine, CNRS, Institut Jean Lamour, UMR 7198, F-54000 Nancy, France
[2] Universidad Carlos III de Madrid, Department of Aerospace Engineering, Leganés, Madrid 28911, Spain
[3] Institut Universitaire de France, Paris, France
[4] Laboratoire de Physique des Plasmas, CNRS, Ecole Polytechnique, Sorbonne Université, Université Paris-Saclay, Observatoire de Paris, 91120 Palaiseau, France
[5] Ecole Polytechnique, Institut Polytechnique de Paris, 91128 Palaiseu, France
[6] Institute of Physics, Ecole Polytechnique Fédérale de Lausanne (EPFL), CH-1015 Lausanne, Switzerland
[7] Center for Quantum Science and Engineering, Ecole Polytechnique Fédérale de Lausanne (EPFL), CH-1015 Lausanne, Switzerland
[8] Research Institute for Applied Mechanics, Kyushu University, Kasuga, Fukuoka 816-8580, Japan
[9] Research Center for Plasma Turbulence, Kyushu University, Kasuga, Fukuoka 816-8580, Japan

E-mail: gcuerva@ing.uc3m.es

Received 28 March 2025, revised 29 May 2025
Accepted for publication 16 June 2025
Published 30 June 2025

Abstract

The presence of impurity ions in magnetically confined plasmas can significantly influence micro-instabilities, impacting cross-field transport and ultimately affecting fusion performance. In particular, Parallel Velocity Gradient (PVG) instability, commonly observed at the edge of fusion devices and in linear devices, can be strongly influenced by impurities. Inspired by the drift-wave models of Hasegawa-Mima and Hasegawa-Watakani, this article develops and examines two distinct fluid models: the ideal impurity-PVG model and the resistive impurity-PVG model. These models aim to investigate the impact of impurities on key properties of the PVG instability, both in the linear and nonlinear regimes. Our findings show that non-negligible impurity concentrations change the growth rates, wave-number ranges, and nonlinear saturations of these instabilities. Notably, the degree of ionization and the relative impurity flow shear can either amplify or mitigate PVG-related turbulence, depending on the impurity and overall plasma conditions. The results underscore the need for a more comprehensive treatment of multi-ion-species plasmas, particularly when impurity fractions cannot be treated as traces.

Keywords: impurities, micro-instabilities, drift-wave turbulence, parallel velocity gradient instability

1. Introduction

Magnetic confinement fusion devices aim to achieve nearly emission-free power generation by sustaining a plasma in which Lawson's criteria are satisfied [1]. However, plasma-facing components and external injections introduce non-hydrogenic ions such as Tungsten or Carbon, which may significantly alter micro-instabilities and cross-field transport. One micro-instability of particular interest is the Parallel Velocity Gradient (PVG) instability, which generates turbulence through radial gradients in parallel plasma flow

* Author to whom any correspondence should be addressed.

and contributes to cross-field transport, including impurity transport [2].

The PVG instability was first studied by D'Angelo under the assumptions of uniform magnetic field and low-beta conditions [3]. It resembles a Kelvin–Helmholtz-(like) mechanism, in which velocity shear drives the growth of electrostatic modes. Subsequently, Catto *et al* [4] identified the roles of density gradients and magnetic shear in stabilizing PVG modes. Subsequent theoretical studies and experimental validations [5–8] confirmed the presence of PVG-driven turbulence at the edges of fusion devices. Similar velocity-shear-driven processes have also been observed in linear devices such as PANTA [9]. Moreover, PVG-driven flows can influence the impurity transport dynamics [2], establishing a connection between impurity transport and the associated turbulent processes in the plasma.

Impurity transport is a key factor in determining plasma performance in fusion devices. Many studies assume the trace impurity limit, where impurity concentrations are low enough to avoid influencing background dynamics. This assumption is supported by experiments-for example, tungsten concentrations above 10^{-4} can cause radiative collapse, making ignition unsustainable [10]. As a result, the trace limit is widely used, particularly for heavy impurities [11–16]. However, it is valuable to examine impurity effects beyond the trace limit [17], particularly within simplified fluid models. Motivated by this, we develop and analyse two reduced two-fluid models that incorporate finite impurity content. The first is an ideal impurity-PVG model based on Boltzmann-response electrons, similar to the Hasegawa–Mima model [18]. The second is a resistive impurity-PVG model that includes parallel resistive dynamics, analogous to the Hasegawa–Wakatani model [19]. While our main focus is low-Z impurities, we also include high-Z species like C^{6+} and W^{40+} to investigate qualitative trends. The impurity concentrations used (e.g. $n_{s0}/n_0 \sim 10^{-3}$) exceed experimental limits for tungsten, and are not intended to model reactor conditions, but rather to assess the sensitivity of impurity effects within the model framework.

The paper is organized as follows: section 2 reviews the derivation and introduces the two multi-ion-species PVG models. Section 3 examines their linear properties, demonstrating how impurities modify dispersion relations and instability boundaries. Section 4 turns to numerical simulations performed via pseudo-spectral codes, verifying linear growth rates and examining nonlinear saturation, turbulence spectra, and coherent structure formation. Finally, section 5 summarizes our findings and discusses the implications for fusion-edge modelling and linear plasma devices.

2. Models

2.1. Fluid approximation and geometry

All models adopt a local Cartesian approximation with basis vectors ($\hat{\boldsymbol{e_x}}$, $\hat{\boldsymbol{e_y}}$, $\hat{\boldsymbol{e_z}}$). The magnetic field is homogeneous and constant, $\boldsymbol{B} = B\hat{\boldsymbol{e_z}}$. Subscripts $\parallel$ and $\perp$ denote directions parallel to $\hat{\boldsymbol{e_z}}$ and within the perpendicular plane ($\hat{\boldsymbol{e_x}}$, $\hat{\boldsymbol{e_y}}$).

Table 1. Normalization scheme.

Quantity	Normalization
Time: t, ω, γ	$\hat{t} = \omega_{c,i} t$
Length: x, y, z, L_n	$\hat{x} = x/\rho_{c,i}$
Velocity: $u_\parallel, <\nabla_\perp u_\parallel>$	$\hat{u_\parallel} = u_\parallel/\rho_i\omega_{\rm ci}$
Potential: ϕ	$\hat{\phi} = e\phi/T_e$

Table 2. Impurity-related parameters.

Parameter	Definition
Mass ratio	$M_s = m_z/m_i$
Concentration	$C_s = n_{s0}/n_0$
Ionization number	$Z_s = e_s/e$

For each species s, the equilibrium density and PVGs are constant, and along x:

$$\boldsymbol{\nabla} n_{s,0} = -\frac{n_{s,0}}{L_{n,s}}\hat{\boldsymbol{e_x}}, \quad \boldsymbol{\nabla} u_{\parallel,s,0} = \frac{u_{\parallel,s,0}}{L_{u,s}}\hat{\boldsymbol{e_x}} \tag{1}$$

where $L_{n,s}$ and $L_{u,s}$ are the respective gradient scale lengths.

We consider a plasma with electrons ($s = e$), a main ion species ($s = i$), and an impurity species ($s = z$), though straightforwardly the model generalizes to additional species. Each species has mass m_s and charge $q_s = Z_s e$, with $Z_e = -1$ and $Z_i = 1$.

The fluid-drift ordering $\epsilon = \omega/\omega_{\rm ci} \ll 1$, where $\omega_{\rm ci}$ is the ion-cyclotron frequency, separates timescales. As a result, ion polarization and viscous drift are second-order corrections to the first-order $\mathbf{E}\times\mathbf{B}$ drift,

$$\boldsymbol{u}_\perp \sim \epsilon\frac{\boldsymbol{E}\times\boldsymbol{B}}{B^2} - \epsilon^2\left(\frac{1}{\omega_{c,s}B}\frac{\mathrm{d}}{\mathrm{d}t}\left(\nabla_\perp\phi\right) + \nu\nabla_\perp\left(\nabla_\perp^2\phi\right)\right) + \ldots \tag{2}$$

where ν is the ion viscosity coefficient, assumed constant across species. Consequently, the total time derivative is dominated by the $\mathbf{E}\times\mathbf{B}$ drift,

$$\frac{\mathrm{d}}{\mathrm{d}t} \sim \frac{\partial}{\partial t} + \boldsymbol{u}_E\cdot\boldsymbol{\nabla}. \tag{3}$$

2.2. Normalization and multi-species effective quantities

We adopt a uniform normalization scheme for all models, as detailed in table 1. Moreover, as we deal with multiple ion species we define impurity-specific parameters, as shown in table 2.

From the inclusion of non-hydrogenic ions, models will include effective quantities for multiple species. The average density gradient length $\frac{1}{\overline{L_n}}$,

$$\frac{1}{\overline{L_n}} = \sum_{s\neq e} Z_s\frac{C_s}{L_{n,s}} \tag{4}$$

and the average mass ratio $\overline{M}$,

$$\overline{M} = \sum_{s\neq e} C_s M_s. \tag{5}$$

2.3. Ideal impurity-PVG model

The ideal impurity PVG model is an extension of the well-known Hasegawa–Mima model, originally developed by Akira Hasegawa and Kunioki Mima in the late 1970s to explain broad frequency spectra of density fluctuations observed in laser experiments [18]. The Hasegawa–Mima model describes drift wave turbulence in a slab geometry with a background density gradient in the x-direction and a constant axial magnetic field. It combines the ion continuity equation-neglecting parallel inertia-with quasi-neutrality and assumes an adiabatic electron response. Building upon this foundation, the ideal impurity PVG model introduces two key modifications. It incorporates multiple ion species, including impurities, and adds the parallel momentum equation for ions, thereby capturing parallel dynamics absent in the original Hasegawa–Mima formulation. Therefore, the general equations for this model are the following,

$$\frac{\partial n_s}{\partial t} + \boldsymbol{\nabla}_\perp \cdot \left[n_s \left(\boldsymbol{u_E} + \boldsymbol{u_{p,s}}\right)\right] + \nabla_\parallel \left(n_s u_{\parallel,s}\right) = 0 \tag{6}$$

$$\sum_{s\neq e} Z_s n_s = n_e = n_0 \exp\left(\frac{e\phi}{T_e}\right) \tag{7}$$

$$\frac{\partial u_{s,\parallel}}{\partial t} + \left(\boldsymbol{u_E} + \boldsymbol{u_{p,s}} + \boldsymbol{u_{\mathrm{visc},s}}\right)\cdot \nabla_\perp u_{s,\parallel} + u_{s,\parallel}\nabla_\parallel u_{s,\parallel} = -\frac{q_s}{m_s}\nabla_\parallel \phi + \mu_\nu \nabla_\parallel^2 u_{s,\parallel} - \mu u_{s,\parallel} \tag{8}$$

where $\mu_\nu \nabla_\parallel^2 u_{s,\parallel}$ is the z-component of the viscous stress tensor following Braginski closure [20], and $-\mu u_{s,\parallel}$ represents the drag coefficient due to ion-neutral collisions [21–23]. Although these terms are not essential for the growth of the instability, they play a crucial role in its physical dissipation during the nonlinear regime.

The linear properties are described in [24, 25], but a summary is provided below. First, 4 terms are neglected:

(i) $\left(\boldsymbol{u_{p,s}} + \boldsymbol{u_{\mathrm{visc},s}}\right)\nabla_\perp n_s \ll \boldsymbol{u_E}\nabla_\perp n_s$ as $\left(\boldsymbol{u_{p,s}} + \boldsymbol{u_{\mathrm{visc},s}}\right)$ is of order $\omega/\omega_{\mathrm{ci}}$ compared to $\boldsymbol{u_E}$.
(ii) $\left(\boldsymbol{u_{p,s}} + \boldsymbol{u_{\mathrm{visc},s}}\right)\nabla_\perp u_{\parallel,s} \ll \boldsymbol{u_E}\nabla_\perp u_{\parallel,s}$ as $\left(\boldsymbol{u_{p,s}} + \boldsymbol{u_{\mathrm{visc},s}}\right)$ is of order $\omega/\omega_{\mathrm{ci}}$ compared to $\boldsymbol{u_E}$.
(iii) $u_{s,\parallel}\nabla_\parallel n_s \ll \frac{\partial n_s}{\partial t}$, $u_{s,\parallel}\nabla_\parallel u_{s,\parallel} \ll \frac{\partial u_{s,\parallel}}{\partial t}$, must remain satisfied to avoid strong Landau damping

Linearizing and combining the density equations gives a single equation for ϕ, while each ion species contributes its parallel velocity equation. In normalized form, this reduces to $s+1$ equations, which we write for clarity as

$$\frac{\partial}{\partial \hat{t}}\left(\hat{\phi} - \overline{M}\nabla_\perp^2\hat{\phi}\right) + \frac{\overline{1}}{L_n}\frac{\partial \hat{\phi}}{\partial \hat{y}} - \overline{M}\left[\hat{\phi}, \nabla_\perp^2\hat{\phi}\right] + \sum_{s\neq e} Z_s C_s \nabla_\parallel \widehat{u_{s,\parallel}} + \nu\nabla_\perp^4\hat{\phi} = 0$$

$$\frac{\partial \widehat{u_{s,\parallel}}}{\partial \hat{t}} - < \nabla_\perp u_{s0,\parallel} > \frac{\partial \hat{\phi}}{\partial \hat{y}} + \left[\hat{\phi}, \widehat{u_{s,\parallel}}\right] = -\frac{Z_s}{M_s}\nabla_\parallel \hat{\phi} + \mu_\nu \nabla_\parallel^2 \widehat{u_{s,\parallel}} - \mu\widehat{u_{s,\parallel}}. \tag{9}$$

The system of equations in equation (9) describes the evolution of the normalized potential, $\hat{\phi}$, and the normalized parallel velocity fluctuations ,$\widehat{u_{s,\parallel}}$. The first equation governs the time evolution of the potential, including its time derivative, perpendicular Laplacian, a gradient term in y-direction, a Poisson bracket, and a sum over ion species weighted by charge state Z_s and $\widehat{u_{s,\parallel}}$. The second equation governs the evolution of $\widehat{u_{s,\parallel}}$, incorporating its time derivative, background velocity gradient, and a Poisson bracket with $\hat{\phi}$. On the right-hand side, it includes the potential gradient response, diffusion, and nonlinear damping. The hyper-dissipative terms, $\nu\nabla_\perp^4\hat{\phi}$, and $mu_\nu\nabla_\parallel^2\widehat{u_{s,\parallel}}$ come from the perpendicular and parallel viscous terms of the stress tensor.

The difference between this model and the one developed in [24] is the inclusion of three extra terms: the viscosity term in the electric potential equation and the viscosity and drag coefficient terms in the parallel flow equations. As demonstrated in the following sections, incorporating these terms is essential for accurately modelling the nonlinear regime of the instability.

The ideal impurity-PVG model is formed on the assumption that electrons follow Boltzmann's distribution, that is why we label it as 'ideal.' Conversely, the forthcoming model we will present, known as the resistive impurity-PVG model, does not rely on that assumption and instead relies on principles of charge conservation and collision between electrons and ions to complete the set of equations.

2.4. Resistive impurity-PVG model

The resistive impurity PVG model is an extension of the Hasegawa–Wakatani model, originally developed by Hasegawa and Wakatani in the early 1980s [19]. The Hasegawa–Wakatani model is a refined version of the Hasegawa–Mima model which incorporated resistivity as a source of dissipation to drive drift wave turbulence [26]. In their formulation, the instability is driven by resistive coupling between electrons and ions, while ion viscosity acts as the dominant dissipation mechanism at both large and small scales. As in the Hasegawa–Mima model, the Hasegawa–Wakatani model assumes a slab geometry, cold ions with negligible parallel inertia, and an adiabatic electron response, but adds a charge balance equation to account for resistive effects.

Extending this framework, the resistive PVG model includes multiple ion species-such as impurities-and incorporates full parallel ion and electron dynamics. For two ion species, $s = i, z$, the model consists of five coupled equations: continuity and parallel momentum equations for each ion species, and a generalized charge conservation equation based on quasineutrality, $\frac{\partial \rho}{\partial t} \sim 0$. Additionally, the electrons are treated as isothermal along the field lines. This extended model captures the interplay between resistivity, parallel flows, and impurity transport.

$$\frac{\partial n_s}{\partial t} + \nabla_\perp \left[n_s\left(\boldsymbol{u_E} + \boldsymbol{u_{p,s}}\right)\right] + \nabla_\parallel\left(n_s u_{s,\parallel}\right) = 0 \tag{10}$$

$$\nabla \cdot \mathbf{J} = \nabla_\perp \mathbf{J}_\perp + \nabla_\parallel J_\parallel = 0 \tag{11}$$

$$m_s n_s \frac{\mathrm{d}u_{s,\parallel}}{\mathrm{d}t} = -e_s n_s \nabla_\parallel \phi + \mu_v \nabla_\parallel^2 u_{s,\parallel} - \mu u_{s,\parallel} - \sum_{s' \neq s} m_{s'} n_{s'} \left(u_{s,\parallel} - u_{s',\parallel}\right) \nu_{s's}. \tag{12}$$

The perpendicular current is determined by the difference in perpendicular velocities between electrons and ions. However, due to the drift approximation, the $\boldsymbol{u_E}$ term on ions and electrons cancels out, leaving only the polarization and viscosity terms of the ions.

$$\boldsymbol{J}_\perp = en_0 \left(\sum_{s\neq e} Z_s \frac{n_{s0}}{n_0} \boldsymbol{u}_{\boldsymbol{s},\perp} - \boldsymbol{u}_{\boldsymbol{e},\perp} \right) \approx en_0 \left(\sum_{s\neq e} Z_s \frac{n_{s0}}{n_0} \left(\boldsymbol{u}_{\boldsymbol{p},s} + \boldsymbol{u}_{\mathbf{visc},s}\right) \right). \tag{13}$$

Due to their low inertia, electrons are assumed to carry most of the parallel current since electron parallel velocity is much greater than the ion parallel velocity $\frac{u_{e,\parallel}}{u_{s,\parallel}} \sim \frac{c_{se}}{c_{ss}} \sim \sqrt{\frac{m_s}{m_e}} \gg 1$. Consequently, the parallel current for impure plasmas takes the form

$$J_\parallel = en_0 \left(\sum_{s\neq e} Z_s \frac{n_{s0}}{n_0} u_{s,\parallel} - u_{e,\parallel} \right) \approx en_0 \left(-u_{e,\parallel}\right). \tag{14}$$

From the electron parallel momentum equation, neglecting the electron inertia term, it is possible to retrieve an expression of the parallel current in terms of the electric potential and density fluctuations,

$$0 \sim -\nabla_\parallel p_e - n_e e E_\parallel + \sum_{s\neq e} m_e \frac{J_\parallel}{e} \nu_{es} \tag{15}$$

where ν_{es} is the electron-ion collision frequency for each ion species, s. The electron-ion collision for each species can be written in terms of the electron-ion collision for a pure plasma ν_{ei},

$$\nu_{es} = Z_s^2 C_s \nu_{ei} \tag{16}$$

where $\nu_{ei} = \frac{e^4 n_0 \ln\Lambda}{(4\pi\epsilon_0)^2 m_e^{1/2} T_e^{3/2}}$ [27]. Rearranging terms, the parallel current can be written as

$$J_\parallel = \frac{T_e}{e\eta_{\mathrm{imp}}} \nabla_\parallel \left(\sum_{s\neq e} Z_s \frac{n_s}{n_0} - \frac{e\phi}{T_e} \right) \tag{17}$$

where η_{imp} is the resistivity of the impure plasma,

$$\eta_{\mathrm{imp}} = \frac{m_e \nu_{ei}}{n_0 e^2} \sum_{s\neq e} Z_s^2 C_s \tag{18}$$

which depends on the ionization number and concentration of impurities.

As previously mentioned, electrons carry most of the parallel current, therefore all ions' parallel-momentum equations share a common structure,

$$\frac{\mathrm{d}u_{s,\parallel}}{\mathrm{d}t} \approx \frac{e_s}{m_s} E_\parallel + \mu_v \nabla_\parallel^2 u_{s,\parallel} - \mu u_{s,\parallel} - \frac{m_e \nu_{ei}}{m_s n_s} Z_s^2 C_s \frac{J_\parallel}{e}. \tag{19}$$

Table 3. Main SPEKTRE parameters [28, 29].

B (mT)	n_0 (m^{-3})	T_e (eV)	T_i (eV)
440	10^{19}	10	1

Including the parallel current given by equation (17), the parallel momentum equation for a given ion species s has the form

$$\frac{\mathrm{d}u_{s,\parallel}}{\mathrm{d}t} = -\frac{Z_s e}{m_s} \nabla_\parallel \phi + \mu_v \nabla_\parallel^2 u_{s,\parallel} - \mu u_{s,\parallel} + \frac{Z_s^2 / M_s}{\sum_{s\neq e} Z_s^2 C_s} \frac{T_e}{m_i} \nabla_\parallel \left(\frac{e\phi}{T_e} - \sum_{s\neq e} Z_s \frac{\widetilde{n_s}}{n_0} \right). \tag{20}$$

Similar to the Hasegawa–Wakatani model, it is possible to retrieve an equation for the electric potential by including the different expressions of parallel and perpendicular currents on the charge conservation. Furthermore, all density equations share a common structure including terms appearing on the charge conservation. Including the ion's parallel momentum equation, this procedure results in a model composed of $2s+1$ equations for s ion species, given by

$$\frac{\partial}{\partial \hat{t}} \left(\frac{\widetilde{n_s}}{n_0} \right) + \frac{C_s}{L_{n,s}} \frac{\partial \hat{\phi}}{\partial \hat{y}} + \left[\hat{\phi}, \frac{\widetilde{n_s}}{n_0} \right] + C_s \nabla_\parallel \widehat{u_{s,\parallel}} = -\frac{C_s M_s / Z_s}{\overline{M}} C_{\mathrm{imp}} \nabla_\parallel^2 \left(\hat{\phi} - \sum_{s\neq e} Z_s \frac{\widetilde{n_s}}{n_0} \right) \tag{21}$$

$$\frac{\partial}{\partial \hat{t}} \left(\nabla_\perp^2 \hat{\phi} \right) + \left[\hat{\phi}, \nabla_\perp^2 \hat{\phi} \right] = -\frac{C_{\mathrm{imp}}}{\overline{M}} \nabla_\parallel^2 \left(\hat{\phi} - \sum_{s\neq e} Z_s \frac{\widetilde{n}}{n_0} \right) + \nu \nabla_\perp^4 \hat{\phi} \tag{22}$$

$$\frac{\partial \widehat{u_{s,\parallel}}}{\partial \hat{t}} - < \nabla_\perp \hat{u_{s0,\parallel}} > \frac{\partial \hat{\phi}}{\partial \hat{y}} + \left[\hat{\phi}, \widehat{u_{s,\parallel}} \right] = -\frac{Z_s}{M_s} \nabla_\parallel \hat{\phi} + \mu_v \nabla_\parallel^2 \widehat{u_{s,\parallel}} - \mu \widehat{u_{s,\parallel}} + \frac{Z_s^2 / M_s}{\sum_{s\neq e} Z_s^2 C_s} \nabla_\parallel \left(\hat{\phi} - \sum_{s\neq e} Z_s \frac{\widetilde{n_s}}{n_0} \right). \tag{23}$$

The system of equations in equations(21)–(23) describes the evolution of the normalized density fluctuations, $\frac{\widetilde{n_s}}{n_0}$, normalized potential, $\hat{\phi}$, and the normalized parallel velocity fluctuations ,$\widehat{u_{s,\parallel}}$. Here, we have included a parameter C_{imp} which is a modified version of the adiabaticity parameter in the conventional Hasegawa–Wakatani model. This parameter depends on plasma resistivity, and therefore is altered by accounting for different collision frequencies,

$$C_{\mathrm{imp}} = \frac{B}{en_0 \eta_{\mathrm{imp}}}. \tag{24}$$

2.5. Model application to linear devices

In the next sections, we will investigate the impurity-PVG instabilities in the linear and non-linear regimes. Let us first introduce the standard parameters adopted in these sections. The plasma parameters are based on the characteristics expected in SPEKTRE [28, 29] (Sheath, Plasma Edge Kinetic Turbulence Radiofrequency Experiment), see table 3.

The baseline values for density gradient length and gradient velocity of main ions are

Table 4. Impurities. Here, $V = \nabla u_{z0,\parallel}/\nabla u_{i0,\parallel}$ is the ratio of parallel velocity gradients.

Impurity	$M = m_z/m_i$	Z	C_z	$L_n/\rho_{c,i}$	V	C_{imp}
W^{40+}	184	40	10^{-3}	10	2	678
W^{5+}	184	5	10^{-3}	10	2	1702
C^{6+}	12	6	10^{-2}	10	2	1336
C^{3+}	12	3	10^{-2}	10	2	1638

$$\frac{L_{n,i}}{\rho_i} = 10, \qquad \frac{< \nabla_\perp u_{\parallel,i0} >}{\rho_i \omega_{\text{ci}}} = 0.07. \tag{25}$$

The value of the density gradient is estimated based on data from similar devices. The parallel shear flow value is an arbitrary but reasonable value above the instability threshold.

Thirdly, the dissipative terms, namely ν, μ_v, and μ, introduced in the models can be computed in their normalized form as

$$\nu = \frac{3}{10}\frac{T_i}{T_e}\frac{\nu_{ii}}{\omega_{\text{ci}}} \sim 7 \cdot 10^{-4} \tag{26}$$

$$\mu_v = \frac{4/3 \cdot (0.96 n_0 T_i/\nu_{ii})}{\rho_i^2 \omega_{\text{ci}}} \sim 6.67 \cdot 10^{-8} \tag{27}$$

$$\mu = \frac{n_0 \sigma_n v_{\text{th}}}{\omega_{\text{ci}}} \sim 0.01. \tag{28}$$

Please note that we assume dissipative terms to remain constant for each of the impurities.

For a multi-species plasma, we will consider that the plasma contains only electrons and two ion species, main-ions $s = i$ and impurity ions $s = z$. We apply our analysis to different impurities ions, which are given in table 4.

In the context of SPEKTRE, we typically focus on low-Z impurities. However, we also include high-Z impurities, such as C^{6+} and W^{40+}. This allows us to gain qualitative trend information that could be relevant for fusion reactor applications, where high-Z impurities may play a role in the plasma behaviour. While the temperature should ideally be adjusted for these higher ionization energies, including such impurities helps provide a broader understanding of impurity physics and their potential impact in fusion environments.

In a multi-species plasma, the main-ion concentration will be $C_i = 1 - ZC_z$. The choice of impurity concentration was made so that the product of Z_s and C_s was of the same order of magnitude for tungsten and carbon. Additionally, based on the information provided in table 4, the adiabaticity parameter undergoes slight modifications for impurities with a low ionization number. However, for high values of Z, there is a substantial change in the parameter C_{imp}. It indicates that the impurity trace approach employed in previous studies may not accurately capture the behaviour of high-Z impurities.

For the shape and grid of the slab geometry, the normalized dimensions are $L_x \times L_y = \frac{4\pi}{3} \times \frac{4\pi}{3}$ with a distribution of grid points $N_x \times N_y = 256 \times 256$.

Unless stated otherwise, the parameters explained above will be used in all of the different analyses that will be shown in the next sections.

In the following sections, we will be studying the linear and nonlinear phases of PVG instability under the effect of impurities. However, we will model the parallel gradient, $\nabla_\parallel$, using a fixed parallel wavenumber. In the linear analysis, we will vary such wavenumber and study the effects of impurities on the maximum growth rate, whereas in the nonlinear analysis, we will select a fixed value and solve numerically the 2D problem. This deliberate approximation is standard in linear studies and enables us to isolate and explore the qualitative influence of impurities on PVG instability within a simplified fluid framework. Nevertheless, we emphasize that this treatment does not capture the full spectrum of parallel dynamics resolved in gyrokinetic simulations. Recent work [15] has shown that retaining the complete parallel operator is essential for accurate transport modelling. Thus, our results should be interpreted as a qualitative approach to how impurities affect the PVG instability rather than quantitatively predictive results.

3. Linear analysis

3.1. Ideal impurity-PVG model

Linearizing the ideal impurity-PVG model results in the dispersion relation shown below

$$\omega^2 - (\omega_{\text{HM,imp}} - \mathrm{i}\,(\mu_{\text{tot}} + \nu_{\text{tot,imp}}))\,\omega - \frac{k_\parallel^2}{1 + \overline{M} k_\perp^2}\left(\overline{c_{ss}^2} - \frac{k_y}{k_\parallel}\overline{< \nabla_\perp u_{0,\parallel} >}\right) - \mu_{\text{tot}}\,(\omega_{\text{HM,imp}} + \nu_{\text{tot,imp}}) = 0. \tag{29}$$

Here, $\omega_{\text{HM,imp}} = \frac{k_y \overline{\frac{1}{L_n}}}{1 + \overline{M} k_\perp^2}$ represents the impurity-modified Hasegawa–Mima dispersion relation, and the effective and dissipative coefficients are defined as:

$$\overline{< \nabla u_{\parallel,0} >} = \sum_{s \neq e} Z_s C_s < \nabla u_{\parallel,s0} >, \qquad \overline{c_{ss}^2} = \sum_{s \neq e} \frac{Z_s^2 C_s}{M_s}$$

$$\mu_{\text{tot}} = \mu + \mu_v k_\parallel^2, \qquad \nu_{\text{tot,imp}} = \frac{\nu k_\perp^4}{1 + \overline{M} k_\perp^2}. \tag{30}$$

Neglecting viscosity and drag coefficients, one can solve the dispersion relation as

$$\omega_{\pm,\text{imp}} = \frac{\omega_{\text{HM,imp}}}{2} \pm \sqrt{\left(\frac{\omega_{\text{HM,imp}}}{2}\right)^2 + \frac{k_\parallel^2}{1 + \overline{M} k_\perp^2}\left(\overline{c_{ss}^2} - \frac{k_y}{k_\parallel}\overline{< \nabla_\perp u_{0,\parallel} >}\right)}. \tag{31}$$

The expression in equation (31) provides insights into the instability mechanisms and the role of impurities. The solution will be unstable, i.e. $\Im\omega_\pm > 0$, if the sum of the terms in the square root becomes less than zero. Leading to a threshold on the effective PVG,

$$\overline{< \nabla_\perp u_{0,\parallel} >} > \frac{k_\parallel}{k_y}\left(\overline{c_{ss}^2} + \frac{1}{4}\frac{\left(\overline{\frac{1}{L_n}}\right)^2}{\left(1 + \overline{M} k_\perp^2\right)\left(\frac{k_\parallel}{k_y}\right)^2}\right) \tag{32}$$

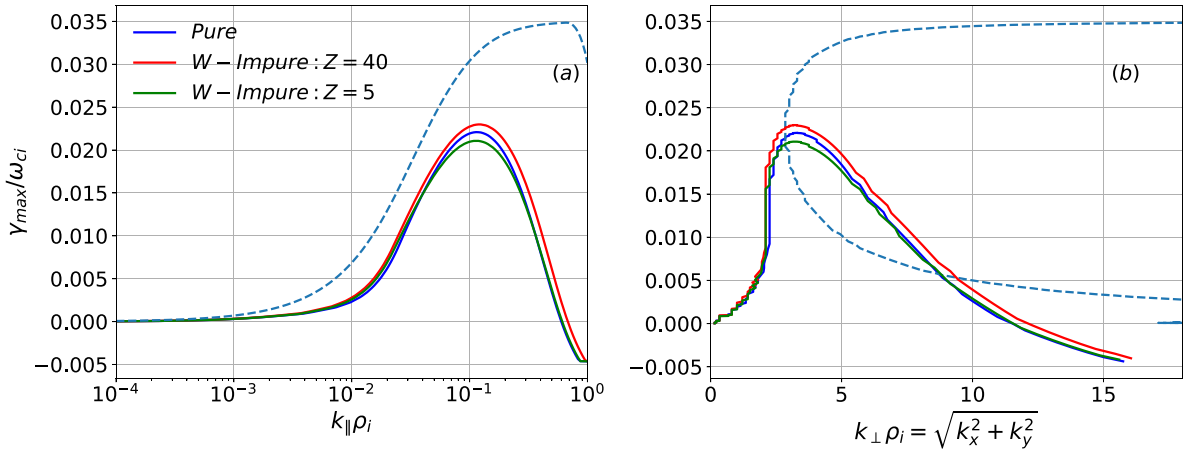

Figure 1. Evolution of maximum growth rate of a Tungsten-impure plasma as a function of (a) parallel wavenumber, $k_\parallel \rho_i$, and (b) perpendicular wavenumber, $k_\perp \rho_i$. The dashed line represents the dispersion relation without drag and viscosity effects.

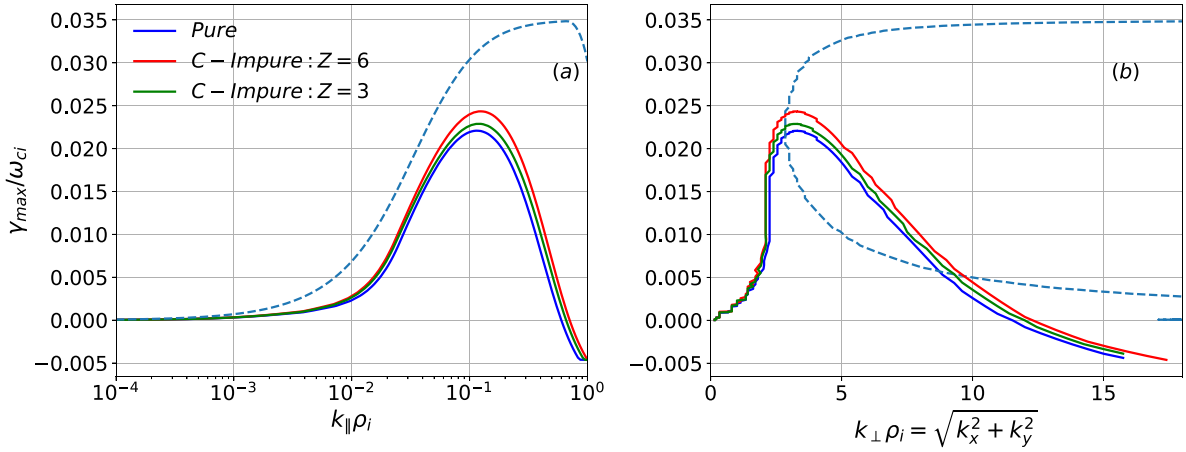

Figure 2. Evolution of maximum growth rate of a Carbon-impure plasma as a function of (a) parallel wavenumber, $k_\parallel \rho_i$, and (b) perpendicular wavenumber $k_\perp \rho_i$. The dashed line represents the dispersion relation without drag and viscosity effects.

When comparing the threshold of the effective PVG with respect to the Kelvin–Helmholtz instability threshold, as given by equation (17) in D'Angelo [3], several important differences arise, primarily due to the inclusion of impurities. First, both the density and velocity gradients are influenced by impurities, making them effective quantities. Second, while the terms $\overline{c_{ss}^2}$ and $\overline{M}$ are equal to one in the pure case (as in D'Angelo), they deviate from one when highly ionized impurities are taken into account.

Another key aspect is that equation (31) describes an instability whose growth rate diverges with $k_\parallel \rho_i$. Numerically, this implies that the choice of the spatial grid determines the maximum growth rate and the localization of the instability in the $k_x\rho_i - k_y\rho_i$ space. This nonphysical behaviour comes from neglecting the viscosity and drag coefficients, ν and μ, which suppressed all sources of dissipation. Therefore, in the following analysis, we study the growth rate from the more complete equation (29).

To address the influence of impurities on the dispersion relation, we first examine the behaviour of the maximum growth rate. Each maximum growth rate corresponds to a specific region within the wavenumber space $(k_x, k_y, k_\parallel)$. However, drawing conclusions from a 3D plot is challenging, so we break down the growth rate evolution in terms of parallel, $k_\parallel$ and perpendicular wavenumbers, $k_\perp = \sqrt{k_x^2 + k_y^2}$, figures 1 and 2.

Figures 1 and 2 show that impurities affect both the growth rate and the extent of the instability region. The presence of impurities alters the effective PVG, which depends on factors such as ionization number and impurity concentration. Hence, different impurities exhibit varying effects on PVG instability. In figures 1(a) and 2(a), we observe that when the product between C_s and Z_s is high enough, the impurities enhance the growth rate of the instability, observed in W^{40+},C^{6+}, and C^{3+} impure plasmas where the growth rate surpasses that of the pure plasma. However, for W^{5+} impurities, the growth rate is reduced compared to pure plasmas. The influence on the region of instability follows a similar trend. For the cases of W^{40+}, C^{6+}, and C^{3+} impure plasmas, the region expands, indicating a lower threshold for PVG destabilization, while for W^{5+}, it remains nearly unchanged.

The effect of the dissipative terms is shown in the evolution of the perpendicular wavenumber, figures 1(b) and 2(b). The

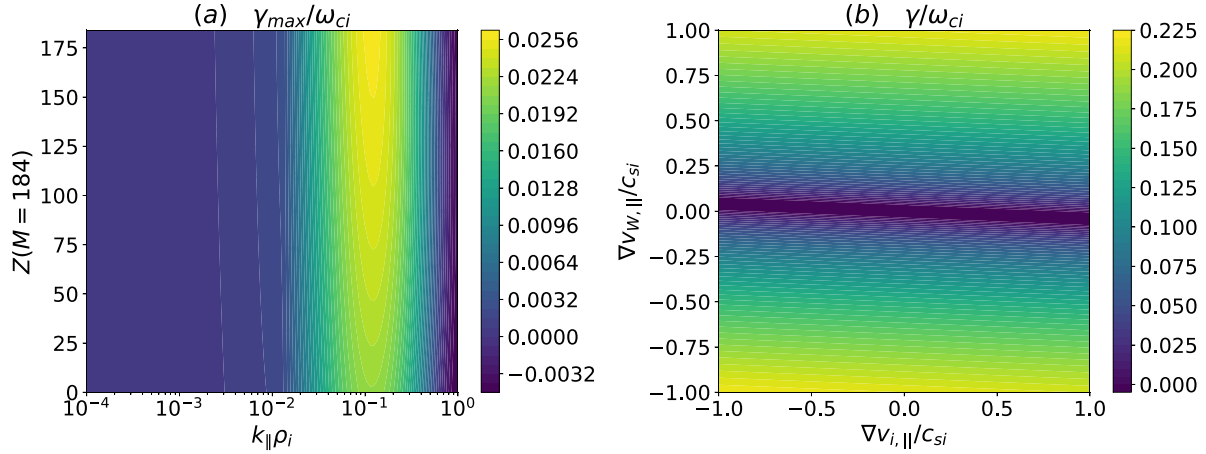

Figure 3. Effect of various parameters on the growth rate of the ideal impurity-PVG model: (a) effect of ionization number on the maximum growth rate, $\gamma_{\max}/\omega_{\rm ci}$, in a W-impure plasma; (b) effect of different V for fixed $k_\parallel \rho_i = 0.06$ in a W^{40+}-impure plasma.

maximum growth rate is approaching zero at small and large scales of $k_\perp \rho_i$ and impurities' effects described before are consistent in these plots. Nonetheless, the values of $k_\perp \rho_i$ reach up to $\sim$15, exceeding the range in which the reduced model used here is formally valid. While these results provide valuable insight, their quantitative accuracy in this regime is limited. This suggests that future work should focus on identifying plasma parameters that allow access to the $k_\perp \rho_i < 1$ regime, where the reduced model remains formally valid.

It is worth noting that in the absence of drag coefficient and ion viscosity, all previous figures have a nonphysical shape, as seen in the dashed lines in figures 1 and 2. In figures 1(a) and 2(a), it is evident that once the instability threshold is surpassed, there is no dissipation mechanism, leading to a positive growth rate for all values of $k_\parallel \rho_i$. Moreover, in figures 1(b) and 2(b), the dashed lines display an unusual shape, with significantly high growth rates for high values of $k_\perp \rho_i$.

Different effective quantities are at play in the PVG instability. In previous graphs, we have maintained the PVGs of main ions and impurities constant, as well as their ionization numbers. Next, we explore their influence on the growth rate, as shown in figure 3.

In figure 3(a), we study the effect of the ionization number while keeping the type of impurity and concentration constant. For this analysis, Tungsten impurities are considered with $C_W = 0.001$, and the maximum growth rate for different values of $k_\parallel \rho_i$ was calculated while varying the ionization number. The behaviour described earlier is demonstrated here, where an increase in Z corresponds to an increase in the growth rate. However, it only surpasses the pure growth rate when $C_s Z_s \gtrsim 0.01$.

Finally, in figure 3(b) we study the effect of the impurity flow shear. Focusing on a specific $k_\parallel \rho_i$ value, we vary the gradient velocities in a W^{40+}-impure plasma. For small values of the impurity PVG, the impurity shear flow amplifies the instability when it has an equal direction to the main ions ($V > 0$), while it stabilizes the system when the flow direction is opposite ($V < 0$).

3.2. Resistive impurity-PVG model

Similarly, linearizing the resistive impurity PVG model results in a dispersion relation, more complex:

$$
\begin{aligned}
&i\omega^3 - \omega^2\left(b_{\rm imp} + \mu_{\rm tot} + \nu k_\perp^2\right) - i\omega\left(\overline{c_{ss}^3} k_\parallel^2 + i b_{\rm imp}\omega_{\rm HM,imp} + b_{\rm imp}\mu_{\rm tot}\right. \\
&\quad \left. + \nu k_\perp^2\left(C_{\rm imp} k_\parallel^2 + \mu_{\rm tot}\right)\right) + b_{\rm imp}\frac{k_\parallel^2}{1+\overline{M}k_\perp^2}\left(\overline{c_{ss}^2} - \frac{k_y}{k_\parallel}\overline{<\nabla_\perp u_{0,\parallel}>}\right) \\
&\quad + \overline{c_{ss}^3}\nu k_\perp^2 k_\parallel^2 + \mu_{\rm tot}\left(i b_{\rm imp}\omega_{\rm HM,imp} + C_{\rm imp} k_\parallel^2 \nu k_\perp^2\right) = 0.
\end{aligned} \tag{33}
$$

Here, $\overline{c_{ss}^3}$ and $b_{\rm imp}$ are multi-species effective quantities defined as:

$$
\overline{c_{ss}^3} = \frac{\sum_{s\neq e}\frac{Z_s^3 C_s}{M_s}}{\sum_{s\neq e} Z_s^2 C_s} \qquad b_{\rm imp} = \frac{C_{\rm imp} k_\parallel^2}{\overline{M}}\frac{1+\overline{M}k_\perp^2}{k_\perp^2}. \tag{34}
$$

The full dispersion relation of the system, given in equation (33), describes two primary instability branches: an impure resistive drift-wave branch and an impure PVG branch. Each of these can be examined separately. The impure resistive drift-wave branch arises from linearizing the impure Hasegawa–Wakatani model and is described by

$$
\omega^2 + i\left(b_{\rm imp} + \nu k_\perp^2\right)\omega - \left(i b_{\rm imp}\omega_{\rm HM,\mathit{imp}} - C_{\rm imp} k_\parallel^2 \nu k_\perp^2\right) = 0. \tag{35}
$$

In contrast, the impure PVG branch reduces to the ideal impurity-PVG model in the limit $C_{\rm imp} k_\parallel^2 \to \infty$, analogous to how the Hasegawa–Mima model is recovered from the Hasegawa–Wakatani model as $C \to \infty$. The corresponding ideal PVG dispersion relation is given in equation (29).

Following the same linear analysis, we obtained the maximum growth rate in the wavenumber space $(k_\perp, k_\parallel)$ for different impure plasmas, figures 4 and 5. The combined influence of the resistivity and PVG is evident in the shape of the maximum growth rate.

The dependence of the maximum growth rate with respect to the parallel wavenumber, figures 4(a) and 5(a), display two

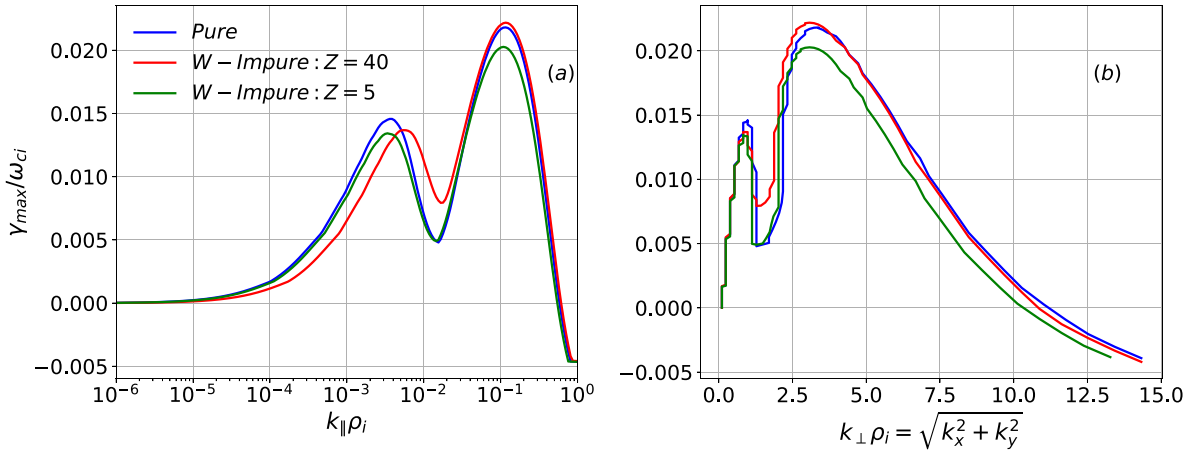

Figure 4. Evolution of maximum growth rate of a Tungsten-impure plasma as a function of (a) parallel wavenumber, $k_\parallel \rho_i$, and (b) perpendicular wavenumber $k_\perp \rho_i$.

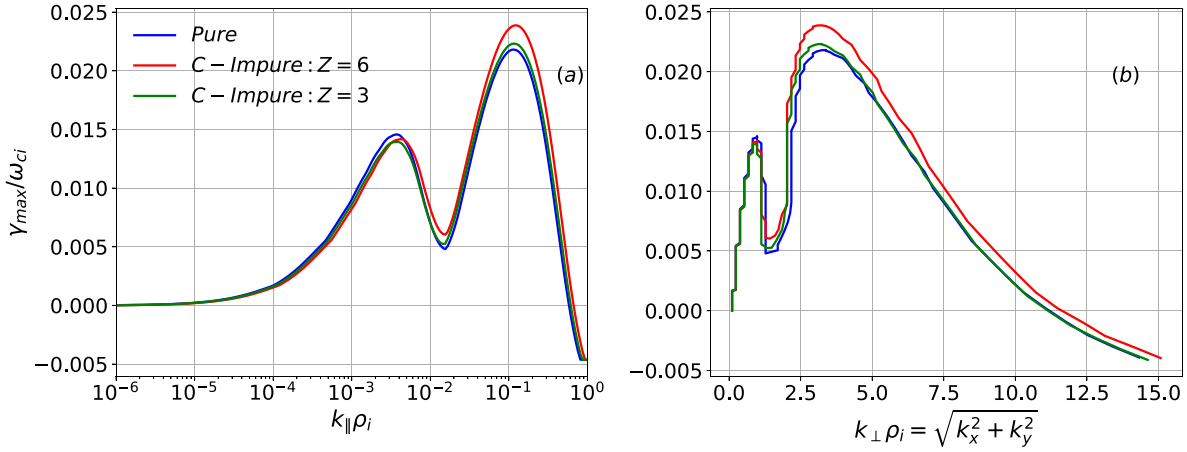

Figure 5. Evolution of maximum growth rate of a Carbon-impure plasma as a function of (a) parallel wavenumber, $k_\parallel \rho_i$, and (b) perpendicular wavenumber $k_\perp \rho_i$.

distinct bell-shaped regions. The first region arises from the resistive drift-wave branch, wherein the peak of the bell shape shifts to higher $k_\parallel \rho_i$ values depending on how much the impurity is ionized. The second region emerges from the PVG, where the impurity type and concentration impact the magnitude of the growth rate, as well as the region of instability. While previous sections presented the results separately, this new model combines both findings, providing a more comprehensive and integrated perspective.

Similarly, the shape of the maximum growth rate as a function of its $k_\perp \rho_i$ location, figures 4(b) and 5(b), is a combination of both models. However, the resistive impurity-PVG model reveals that the region of instability extends over a wider range of wavenumbers compared to previous models. Moreover, including impurities further expands this region, emphasizing the significant impact of impurities on the instability.

We note, however, that in this extended regime, $k_\perp \rho_i$ reaches values beyond unity, where the assumptions underlying the current fluid model begin to break down. While the observed trends remain insightful, caution is warranted in interpreting the results quantitatively at large $k_\perp \rho_i$. This suggests that future work should focus on identifying plasma parameters that allow access to the $k_\perp \rho_i < 1$ regime, where the reduced model remains formally valid.

Lastly, the effects of the ionization number and the impurity flow shear on the growth rate are still of interest and are explored in the analysis, figure 6. We begin by examining the effect of impurity flow shear on different branches of the resistive PVG model. In figure 6(a), we focus on the resistive-drift wave branch. For low values of flow shear, $\nabla u_{0,\parallel}/c_{si} \leqslant \pm 0.25$, the growth rate undergoes slight modifications, and the impurities enhance the instability only when they have the same direction as the main ions ($V > 0$). However, as the flow shear magnitude increases, the growth rate experiences a significant increase, nearly tripling in magnitude. As for the PVG branch, figure 6(b), we observe similar trends to the ideal PVG model: for small values of the PVG, the impurity shear flow amplifies the instability when it has an equal direction to the main ions ($V > 0$), while it stabilizes the system when the flow direction is opposite ($V < 0$). However, when the flow shear becomes very large, this distinction becomes less pronounced, and the growth rate of the instability increases.

In figure 6(c), we explore the impact of the ionization number on the maximum growth rate. Unlike the ideal

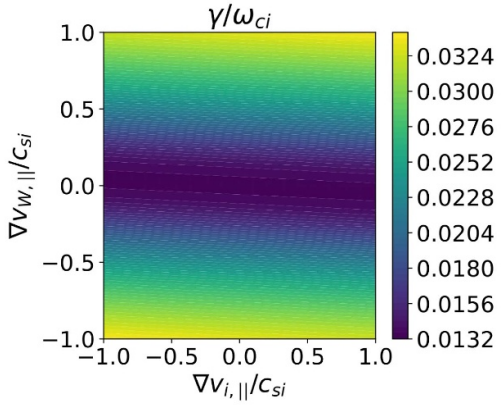

(a) Effect of different V at the resistive drift-wave branch, at $k_{||}\rho_i \sim 0.006$.

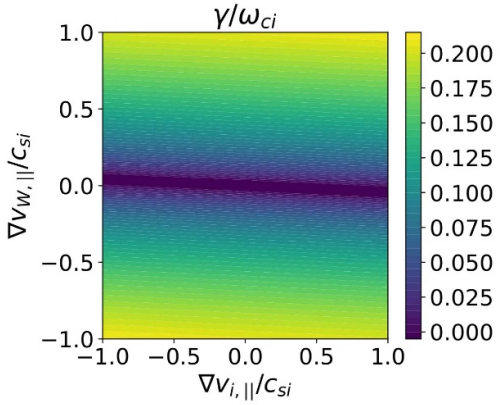

(b) Effect of different V at the PVG branch, at $k_{||}\rho_i \sim 0.116$.

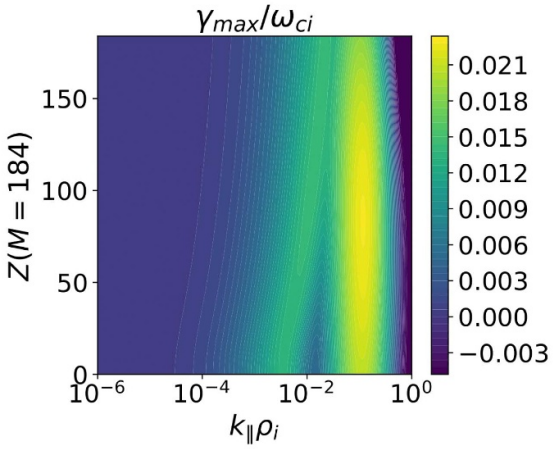

(c) Effect of ionization number on γ_{max}/ω_{ci}.

Figure 6. Effect of various parameters on the growth rate of the resistive PVG model, on a W^{40+}-impure plasma.

impurity-PVG, where an increase in the ionization number leads to a monotonic increase in the maximum growth rate, the resistive impurity-PVG shows a more complex behaviour. As the ionization number plays a major role in the resistivity of the plasma, an increase in resistivity affects the growth rate in both the resistive-drift wave branch and the PVG branch. The plot reveals two significant effects. Firstly, there is a shift in the $k_{||}\rho_i$ location where the maximum growth rate occurs for each branch. The shift suggests that resistivity affects the spatial characteristics of the instability. Secondly, in the PVG branch, a critical limit on the ionization number is observed, beyond which the resistivity becomes significantly large, leading to a reduction of the maximum growth rate.

This linear analysis of the resistive impurity-PVG and ideal impurity-PVG models attests that impurities play a significant role in shaping the behaviour of PVG instability. In the ideal impurity-PVG model, impurities primarily influence the magnitude and region of the growth rate, highlighting the importance of the impurity type and concentration. Furthermore, the introduction of impurities in the resistive impurity-PVG model introduces a more intricate relationship, as they not only impact the growth rate but also modify the plasma resistivity. The interaction between impurities and resistivity leads to changes in both the growth rate and the location of the instability. Consequently, the combined effect of impurities and resistivity generates a more realistic and complex scenario, providing valuable insights into the behaviour of impure PVG instability.

Figure 7 provides a comprehensive overview of the different models utilized in this study for a W^{40+}-impure plasma. Firstly, the ideal impurity-PVG without dissipation terms (green line), initially derived in [24], showcases that the growth rate grows without bounds after the threshold is fulfilled. Secondly, the new ideal impurity-PVG derived in this paper, incorporating dissipation terms, exhibits a bounded region of instability. Finally, the resistive impurity-PVG also developed in this article, incorporates the effects of plasma resistivity and dissipation. The influence of resistivity is evident on the PVG branch, as the resistive PVG has a lower growth rate than the ideal PVG in that region. Although these results

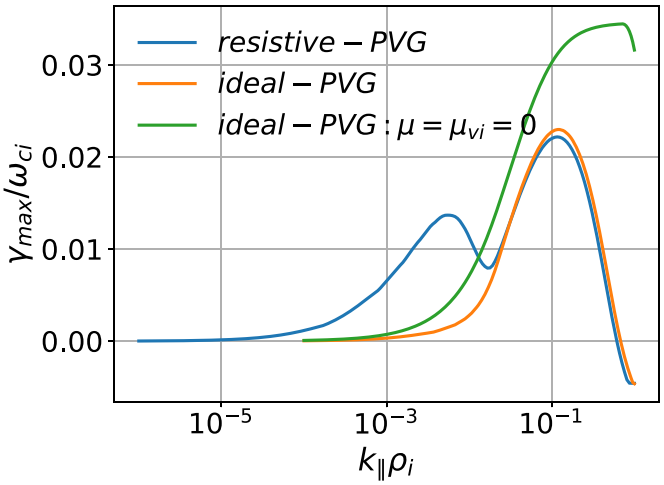

Figure 7. Summary of impure PVG instability for W^{40+}-impure plasma.

capture important trends, the values of $k_\perp \rho_i$ explored here extend beyond the model's strict validity range, and quantitative conclusions in this regime should therefore be treated with caution.

4. Nonlinear analysis

This section investigates the nonlinear dynamics using in-house pseudo-spectral codes for each model.

These pseudo-spectral codes are characterized by using a fourth-order Runge–Kutta time-stepping scheme and Fourier expansions in the perpendicular plane (x, y). A 2/3 de-aliasing rule is applied, and periodic boundary conditions are enforced in the perpendicular sections. The simulations are performed on a grid of size $N_x \times N_y = 256 \times 256$. The fluctuating quantities are initialized with a set of randomly distributed modes of varying amplitude and phase. We will focus on W^{40+} and C^{6+} impure plasmas, at a fixed $k_\parallel \rho_i$ value, corresponding to the position of maximum growth rate in figures 1, 2, 4 and 5. Moreover, ions are initialized with a density and PVGs given in equation (25), while impurities density and PVGs are given in table 4.

We first evaluate the accuracy of the numerical codes by comparing the simulated results to the theoretical dispersion relations in the linear regime. Then, we explore the behaviour in the nonlinear regime, investigating the formation of coherent structures, their magnitudes, and sizes, both in the physical and spectral domains. Instead of comparing our simulations directly to experimental data, we focus on understanding the system's fundamental dynamics and characteristics.

4.1. Ideal impurity-PVG model

We begin by performing numerical simulations on the ideal impurity-PVG model. The simulation parameters as well as the plasma conditions were depicted in section 2.5.

Firstly, the time evolution of the four modes with the highest growth rate is shown in figure 8. Displaying the ability of the code to reach the non-linear regime, where the unstable modes saturate at low amplitudes.

Table 5 compares the numerical growth rates with the theoretical growth rates from the dispersion relation, showing that the relative errors of each simulation stay below 0.1%, indicating high accuracy in simulating the growth of impure-PVG unstable modes in the linear regime. The four highest growth rate modes selected for the comparison have perpendicular wavenumbers $k_\perp \rho_i \sim 3$. While this value is somewhat above the strict $k_\perp \rho_i \lesssim 1$ ordering assumed in the fluid model, it remains within a moderate range where the qualitative features of the instability are expected to be reasonably captured. Nonetheless, we advise caution in interpreting quantitative results at these scales.

Figure 9 illustrates the evolution of the fluctuating electric potential at different simulation times. The left subplot presents a combination of modes having random amplitude and phase without any specific order or pattern. As time progresses, in the middle subplot, the unstable modes grow and approach the nonlinear regime where the modes begin to saturate and form small coherent structures. In the right subplot, these structures interact and grow in size, forming larger patterns. The behaviour of a C-impure plasma follows a similar trend.

Analysing the behaviour of fluctuation quantities in the spectral domain provides valuable insights into both the linear and nonlinear regimes. During the linear regime, the unstable modes will dominate in the spectrum of $e\phi_k/T_e$, hence it is possible to obtain a contour of the numerical dispersion relation. In the nonlinear regime, the time-average spectrum $e\phi_k/T_e$ gives valuable insights into the interaction of the unstable modes and which of them contribute the most in the turbulent regime. Figure 10 displays both the linear and nonlinear spectrum of the numerical simulation along with the theoretical dispersion relation for a W-impure plasma. The behaviour of a C-impure plasma follows a similar trend.

In the linear regime, shown in figures 10(a) and (b), the accuracy of the code is demonstrated by comparing the theoretical dispersion (figure 10(a)) with the numerical spectrum (figure 10(b)) at a fixed time during the linear phase. In this phase, the spectrum is dominated by the growing unstable modes, allowing for a direct comparison with the theoretical growth rate contours in the $k_x\rho_i - k_y\rho_i$ space. The simulation closely matches the theoretical contours; however, it is important to note that grid resolution plays a crucial role in this accuracy. A finer grid would yield a closer match, but achieving this requires a highly parallelized code, which is not implemented in the current version. In the nonlinear regime, figure 10(c), the modes contributing most to turbulence are concentrated in three distinct regions: an upper region with $k_y\rho_i \sim 2$ and $k_x\rho_i \in [-2, 2]$, and two symmetric regions at $k_x\rho_i \sim \pm 1.5$ and $k_y\rho_i \in [-1, 1]$.

4.2. Resistive impurity-PVG model

In the resistive PVG model, we split the code to separately handle the impurity resistive-drift branch at small $k_\parallel \rho_i$, and the

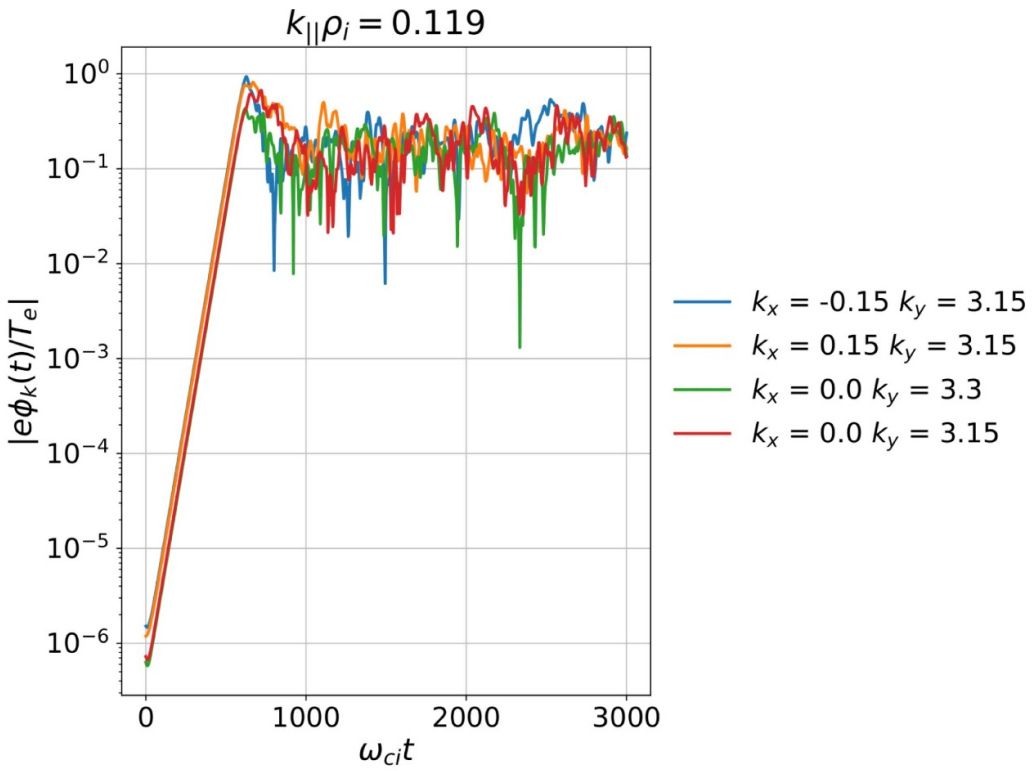

(a) W^{40+}-impure plasma.

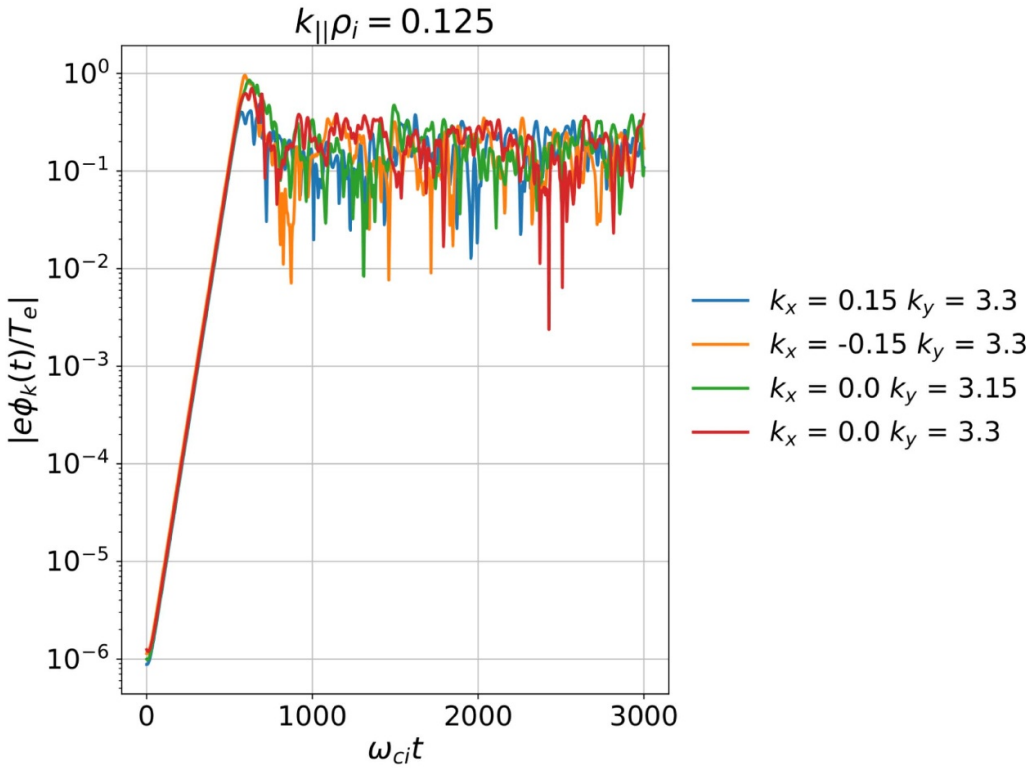

(b) C^{6+}-impure plasma.

Figure 8. Behavior of modes with highest growth rates for different impure plasmas.

Table 5. Comparison of the simulated and theoretical growth rate from the four highest growth rates.

W^{40+}-Impure: $(k_x, k_y, k_\parallel)\,\rho_i$	$\gamma_{\rm th}/\omega_{\rm ci}$	$\gamma_{\rm sim}/\omega_{\rm ci}$	Relative error [%]
$(-0.15, 3.15, 0.119)$	0.022 9523	0.022 9662	0.060 67
$(0.15, 3.15, 0.119)$	0.022 9523	0.022 9669	0.063 76
$(0.0, 3.3, 0.119)$	0.022 9549	0.022 9544	0.002 35
$(0.0, 3.15, 0.119)$	0.022 9863	0.022 9853	0.004 28
C^{6+}-Impure: $(k_x, k_y, k_\parallel)\,\rho_i$	$\gamma_{\rm th}/\omega_{\rm ci}$	$\gamma_{\rm sim}/\omega_{\rm ci}$	Relative error [%]
$(0.15, 3.3, 0.125)$	0.024 3105	0.024 3253	0.060 76
$(-0.15, 3.3, 0.125)$	0.024 3105	0.024 3238	0.054 54
$(0.0, 3.15, 0.125)$	0.024 3164	0.024 3159	0.002 17
$(0.0, 3.3, 0.125)$	0.024 3445	0.024 344	0.002 12

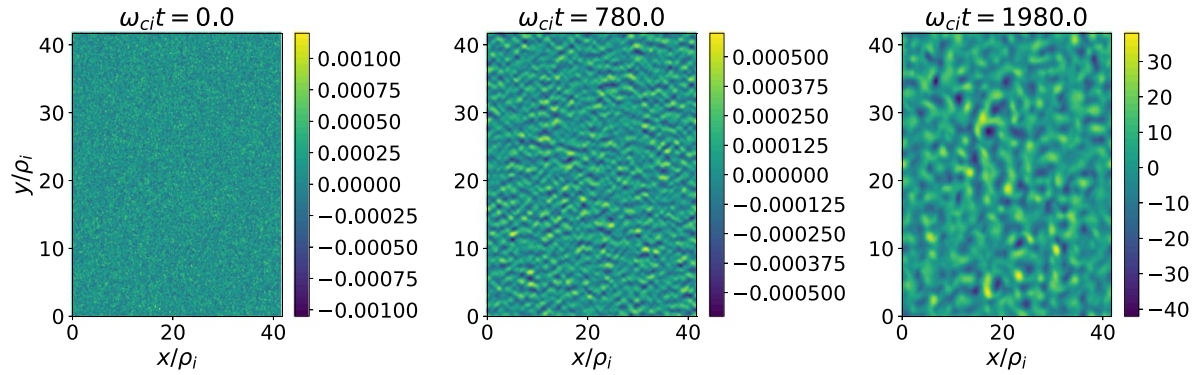

Figure 9. Evolution of the normalized potential, $\tilde{\phi}$, for the ideal PVG instability in a W^{40+}-impure plasma with $k_\parallel \rho_i = 0.119$.

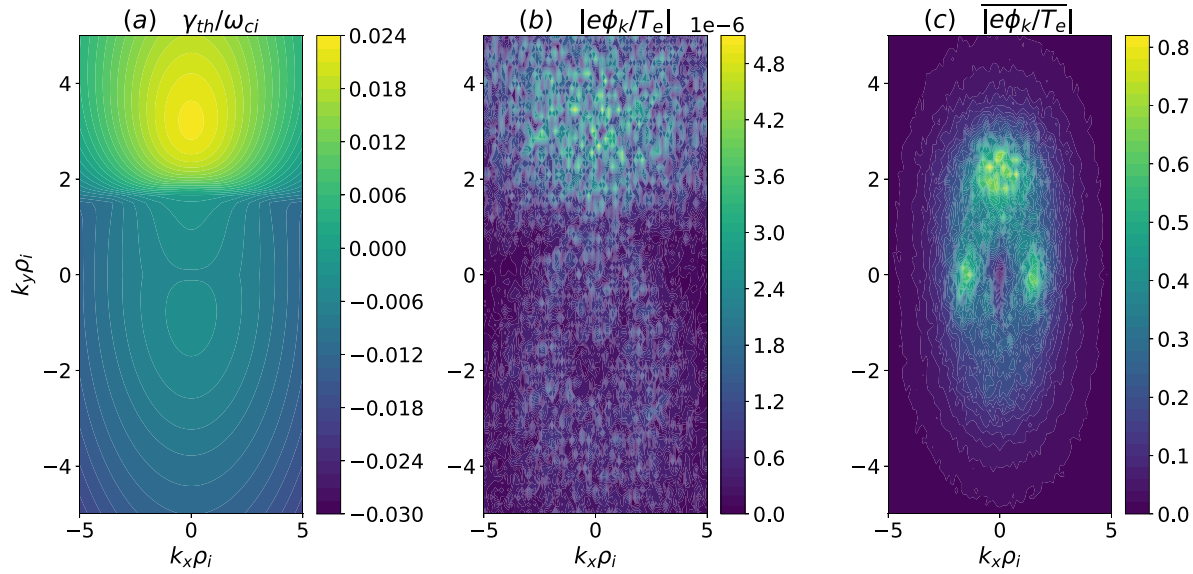

Figure 10. Evolution of PVG instability in a W^{40+}-impure plasma with $k_\parallel \rho_i = 0.119$ in the spectral domain: (a) theoretical dispersion relation from equation (29), (b) $\tilde{\phi}_k$ spectrum in the linear phase, and (c) time-averaged spectrum, $\overline{\tilde{\phi}_k}$, over the nonlinear phase.

ideal impurity PVG branch at large $k_\parallel \rho_i$. This simplification introduces a slight reduction in accuracy for both the linear and nonlinear regimes. Resulting in a few percent error in the linear growth rates, and neglecting the nonlinear effects of PVG in the resistive branch and vice versa. Nevertheless, it still effectively captures the influence of impurities, the overall dynamics, and turbulence generation, which are the primary focus of the study.

Based on the numerical simulations of each branch at different parallel wavenumber values, we present the time evolution of the two modes with the highest growth rates for each branch. Figure 11 demonstrates the code's ability to reach

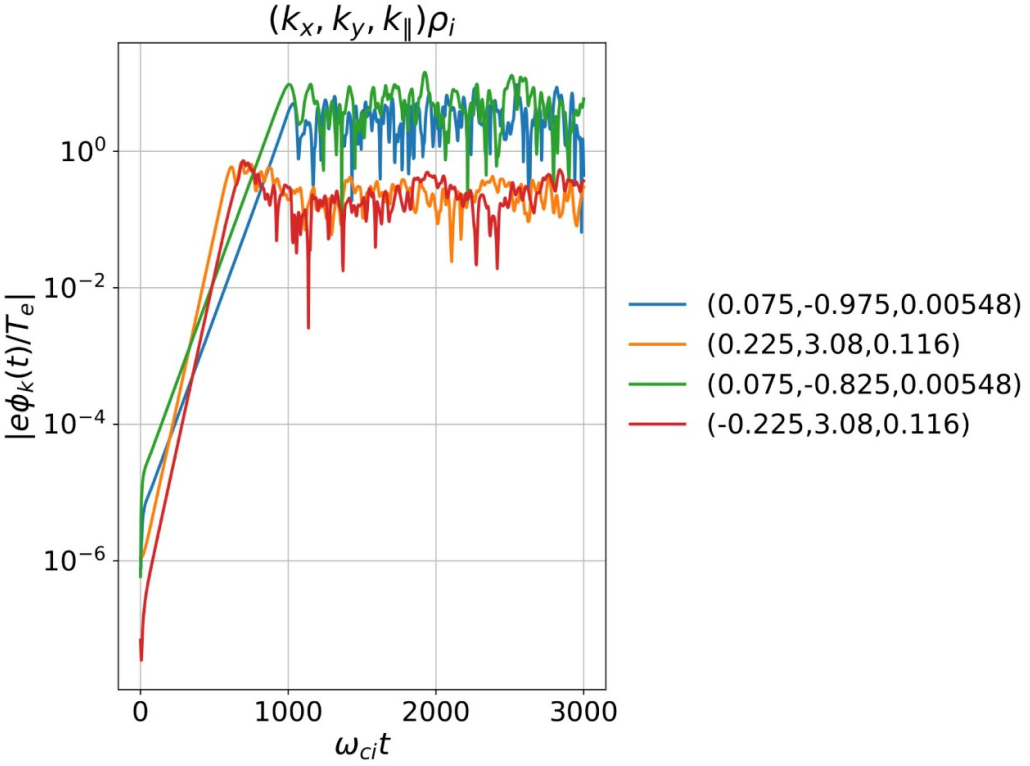

(a) W^{40+}-impure plasmas

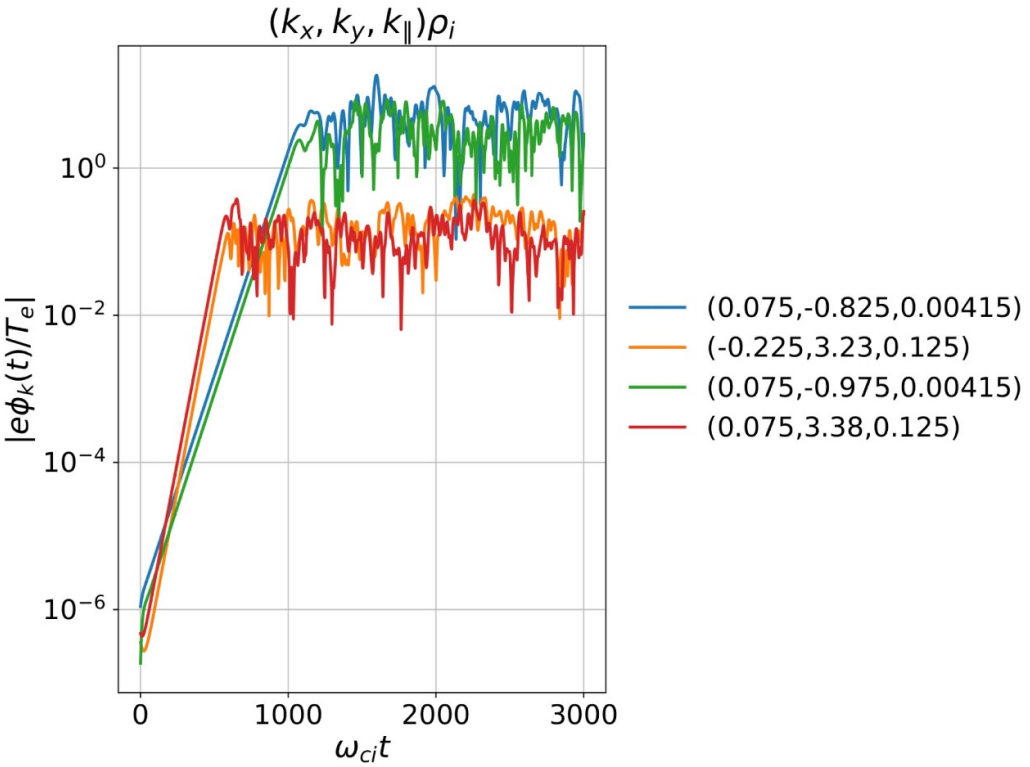

(b) C^{6+}-impure plasma

Figure 11. Behaviour of modes with highest growth rates for different impure plasmas.

Table 6. Comparison of the simulated and theoretical growth rate from the four highest growth rates.

W^{40+}-Impure: $(k_x, k_y, k_\parallel)\,\rho_i$	$\gamma_{\rm th}/\omega_{\rm ci}$	$\gamma_{\rm sim}/\omega_{\rm ci}$	Relative error [%]
$(0.075, -0.975, 0.00548)$	0.013 5429	0.013 5786	2.93
$(0.075, -0.825, 0.00548)$	0.013 6336	0.013 6383	3.12
$(0.225, 3.08, 0.116)$	0.022 1826	0.022 8097	3.16
$(-0.225, 3.08, 0.116)$	0.022 1826	0.022 8709	3.44
C^{6+}-Impure: $(k_x, k_y, k_\parallel)\,\rho_i$	$\gamma_{\rm th}/\omega_{\rm ci}$	$\gamma_{\rm sim}/\omega_{\rm ci}$	Relative error [%]
$(0.075, -0.825, 0.00415)$	0.014 0244	0.014 0436	3.04
$(0.075, -0.975, 0.00415)$	0.014 1461	0.014 1881	0.3
$(-0.225, 3.23, 0.125)$	0.023 7631	0.024 0036	1.01
$(0.075, 3.38, 0.125)$	0.023 7699	0.023 8013	0.13

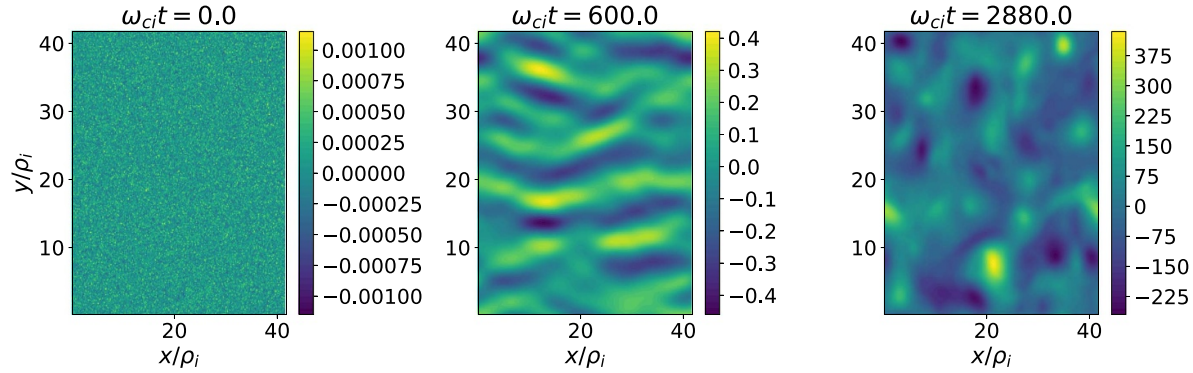

Figure 12. Evolution of the normalized potential, $\tilde{\phi}$, for the resistive PVG instability in a W^{40+}-impure plasma in the resistive branch $k_\parallel \rho_i = 0.00548$.

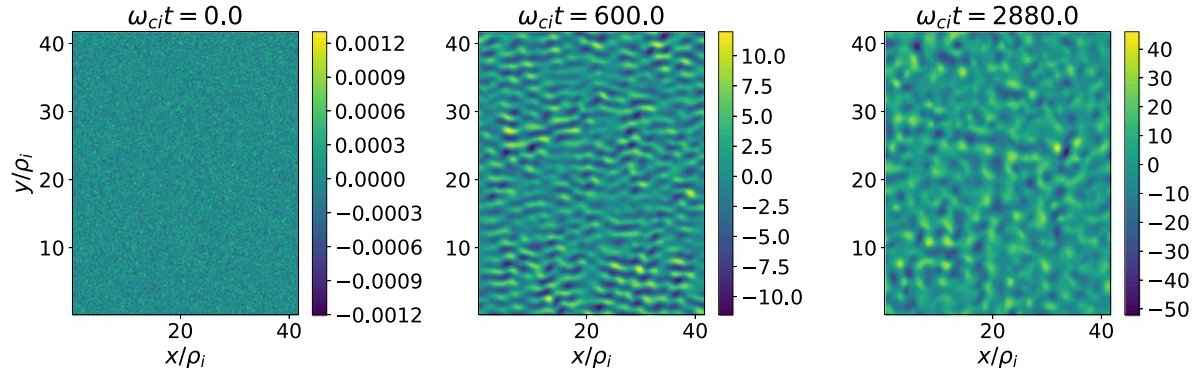

Figure 13. Evolution of the normalized potential, $\tilde{\phi}$, for the resistive PVG instability in a W^{40+}-impure plasma in the PVG branch $k_\parallel \rho_i = 0.116$.

the nonlinear regime in both the resistive drift-wave instability and PVG instability scenarios.

Table 6 compares the numerical growth rates with the theoretical growth rates from the dispersion relation. Unfortunately, splitting the simulation code to solve either the impurity Hasegawa–Wakatani or the ideal PVG model results in higher relative errors in the linear regime. Indeed, our code considers only resistivity in the resistive drift-wave branch and only PVG in the PVG branch, while in reality, both mechanisms influence the growth at each branch. As a result, the accuracy of our simulation is reduced to relative errors ranging from 0.3% to 3.44%, making it less accurate compared to ideal impurity-PVG code.

For the resistive drift-wave branch, the modes with the highest growth rates correspond to perpendicular wavenumbers $k_\perp \rho_i$ generally below unity, thus remaining well within the formal validity range of the fluid model. In contrast, the highest growth rate modes in the PVG branch typically have $k_\perp \rho_i \sim 3$. While this exceeds the strict ordering assumed in the model, it still falls within a moderate range where trends can be informative, though quantitative results should be interpreted with caution.

Figures 12 and 13 show three snapshots of the simulation, illustrating the distinct evolution of electric potential fluctuations at different $k_\parallel \rho_i$ values for a W^{40+} impure plasma. The initial conditions of the fluctuating potential show modes

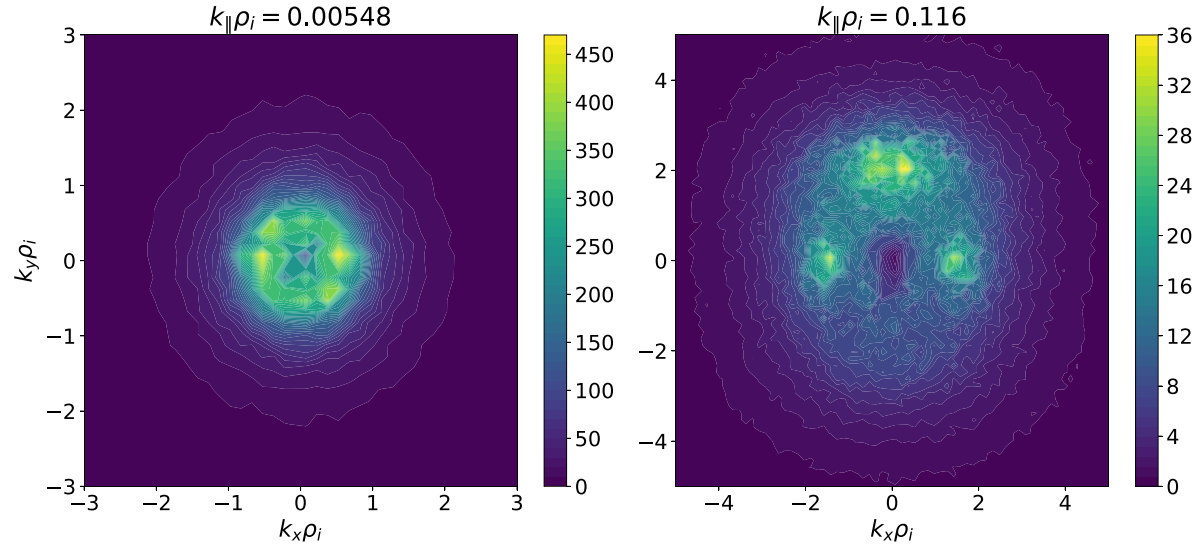

Figure 14. Time-averaged spectrum, $\overline{\tilde{\phi}_k}$, over the nonlinear phase for each branch for a W^{40+}-impure plasma.

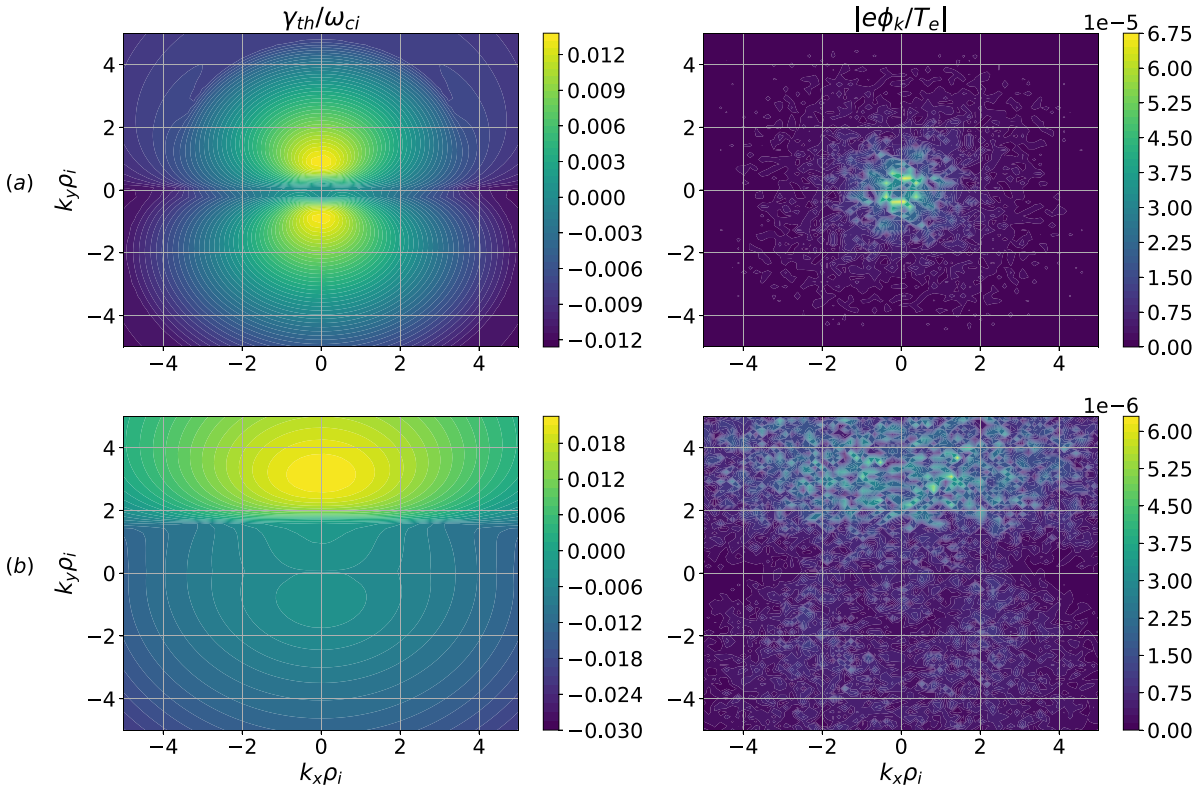

Figure 15. Comparison of $\tilde{\phi}_k$ spectrum in the linear phase with the theoretical dispersion relation from equation (33), γ_{th}, for W^{40+} impure plasma in: (a) the resistive branch and (b) the PVG branch.

with random amplitudes and phases, displaying no specific ordering pattern. The second subplot in both figures illustrates the early stages of the nonlinear regime for the resistive drift-wave and PVG branches, where small eddies begin to form. A noticeable difference is observed in the size of the structures: those in the resistive drift-wave branch are larger than those in the PVG branch. As time progresses, fully developed turbulence is visible in both branches, with the vortices in the resistive drift-wave branch exhibiting larger sizes and greater magnitude compared to those driven by the PVG. This behaviour can be attributed to the dynamics of the impure breather [30], which influences the formation and growth of structures in the resistive drift-wave branch.

Finally, we examine the evolution of the fluctuating potential in the spectral domain, figures 14 and 15. Here, we focus on the simulation of W^{40+} impure plasma, as the results for

C^{6+} exhibit a similar trend. In figure 14, we examine the time-averaged spectrum over the non-linear phase in both branches. The unstable modes responsible for turbulence exhibit similar placement to those observed in the Hasegawa–Wakatani and ideal PVG models. In the resistive drift wave branch, these modes are concentrated within a small circular region characterized by $k_x\rho_i = k_y\rho_i \in [-1, 1]$. On the other hand, in the PVG branch, the unstable modes are spread across a larger circular area, featuring three regions of high intensity.

In figure 15, we illustrate the shape of $e\phi_k/T_e$ in the linear phase and compare it to the growth rate obtained from the dispersion relation for both branches, see equation (33). Similar to the ideal PVG code, the limited grid resolution results in a contour that resembles the theoretical shape but lacks accuracy and resolution. However, we also encounter a noticeable difference in the resistive branch. The influence of the PVG changes the shape of the theoretical contour by increasing its size and including negative growth rates. The simulated contour does not exhibit this behaviour, as the effect of the PVG is neglected, resulting in a shape that resembles the contour of the Hasegawa–Wakatani model.

5. Conclusions

We have developed and analysed two-fluid models to explore the impact of non-trace impurities on PVG-driven instability and turbulence in magnetically confined plasmas, including collisional and dissipative terms.

In the linear regime, we studied how the dispersion relation was affected by impurities. Overall, we observed that impurities indeed affect the frequency and growth rate of the instability, but their effect is different for each model and is highly dependent on the type of impurity and how much is ionized. In the ideal impurity-PVG model, the impurities alter the effective PVG and modify the threshold for instability. For sufficiently large values of C_sZ_s, it can boost growth rates and expand the instability region in wave-number space, whereas lower-ionization or concentration impurities have comparatively modest impacts. Lastly, the direction of the impurity's shear flow is also important, for equal direction to main-ions will enhance the instability, while in the opposite direction, impurities stabilize the system. In the resistive PVG, the interplay between velocity-shear and resistive drift-wave dynamics further enrich the instability landscape. In the resistive drift wave branch, impurities change the resistivity and move the unstable region towards higher $k_\parallel\rho_i$ values, whereas, in the PVG branch, they increase the growth rate and expand the area of instability. However, both resistivity and PVG mechanisms have an impact on the other branch as well. Impurity' shear flow will slightly enhance the growth rate at the resistive drift wave branch for equal direction to main-ions, whereas it slightly reduces it for the opposite direction. In the PVG branch, resistivity yields a certain ionization limit until which impurities amplify the growth rate of the PVG branch. However, as ionization increases further, resistivity begins to affect the growth rate by reducing it.

While our fluid models provide valuable insights, we note that in some parameter regimes, the analysis reaches values of $k_\perp\rho_i$ up to ~ 15, which exceeds the strict validity of the fluid approximation based on the $k_\perp\rho_i \lesssim 1$ ordering. As such, quantitative accuracy in this high-wavenumber regime cannot be guaranteed. However, the observed trends remain suggestive, and this behaviour points to the need for exploring parameter ranges where the instability remains within the low-$k_\perp\rho_i$ regime to ensure consistency with model assumptions.

Nonlinear simulations confirm the key predictions from the linear analysis and highlight the formation of distinct coherent structures in each branch. The results emphasize the importance of going beyond the trace-impurity approximation when impurity fractions become significant, $C_sZ_s \geqslant 0.01$, or when high-ionization states strongly affect resistivity. Moreover, notable differences in eddy size and intensity emerge, reflecting the dominant instability mechanisms. In particular, the resistive branch exhibits larger eddies compared to the PVG branch. Additionally, the spatial organization of unstable modes responsible for eddy formation varies, leading to more diverse turbulence characteristics in the PVG branch. In conclusion, our simplified fluid approach offers insights into how impurities can reshape the PVG instability spectrum and saturation mechanisms.

Data availability statement

All data that support the findings of this study are included within the article (and any supplementary files).

Acknowledgments

This work was supported by funding from the Agence Nationale de la Recherche for the Project GRANUL (ANR-19-CE30-0005) and from Institut Universitaire de France. This work was granted access to the HPC resources of EXPLOR (Project No. 2017M4XXX0251).

References

[1] Lawson J D 1957 *Proc. Phys. Soc. B* **70** 6
[2] Guo W, Wang L and Zhuang G 2019 *Nucl. Fusion* **59** 076012
[3] D'Angelo N 1965 *Phys. Fluids* **8** 1748
[4] Catto P J, Rosenbluth M N and Liu C S 1973 Parallel velocity shear instabilities in an inhomogeneous plasma with a sheared magnetic field *Phys. Fluids* **16** 1719–29
[5] Garbet X *et al* 1999 *Phys. Plasmas* **6** 3955
[6] McCarthy D 2002 *Phys. Plasmas* **9** 2451
[7] Wang G *et al* 1998 *Plasma Phys. Control. Fusion* **40** 429
[8] Chapman I, Brown S, Kemp R and Walkden N 2012 *Nucl. Fusion* **52** 042005
[9] Inagaki S *et al* 2016 *Sci. Rep.* **6** 22189
[10] Pütterich T *et al* 2010 *Nucl. Fusion* **50** 025012
[11] Angioni C and Peeters A G 2006 *Phys. Rev. Lett.* **96** 095003
[12] Futatani S, Garbet X, Benkadda S and Dubuit N 2010 *Phys. Rev. Lett.* **104** 015003

[13] Bourdelle C *et al* 2007 *Phys. Plasmas* **14** 112501
[14] Fable E, Angioni C and Sauter O 2009 *Plasma Phys. Control. Fusion* **52** 015007
[15] Xu S, Maeyama S, Watanabe T-H and Gürcan O D 2024 *Phys. Rev. Lett.* **132** 105101
[16] Angioni C 2021 *Plasma Phys. Control. Fusion* **63** 073001
[17] Lesur M *et al* 2020 *Nucl. Fusion* **60** 036016
[18] Hasegawa A and Mima K 1977 *Phys. Rev. Lett.* **39** 205
[19] Hasegawa A and Wakatani M 1983 *Phys. Rev. Lett.* **50** 682
[20] Braginskii S (edited by M.A Leontovich (Consultants Bureau, New York)) 1965 *Rev. Plasma Phys.* **1** 205
[21] Sasaki M *et al* 2017 *Plasma Fusion Res.* **12** 1401042
[22] Sasaki M *et al* 2019 *Nucl. Fusion* **59** 066039
[23] Sasaki M *et al* 2019 *Phys. Plasmas* **26** 042305
[24] Bourgeois J, Lesur M, Lazaro G C and Kosuga Y 2024 *Open Plasma Sci.* **1** 1
[25] Lesur M, Bourgeois J and Kosuga Y 2023 Fusion Energy 2023 *Proc. 29th Int. Conf. London (IAEA, International Centre)*
[26] Hasegawa A and Mima K 2018 *Eur. Phys. J.* H **43** 499–521
[27] Chen F 2019 *Introduction to Plasma Physics and Controlled Fusion* (Springer)
[28] Brochard F *et al* 2023 *Proc. 49th EPS Conf. on Plasma Physics* (Bordeaux, France)
[29] Gravier E *et al* 2024 *Phys. Plasmas* **31** 112104
[30] Kosuga Y, Bourgeois J, Lesur M and Oyama I 2024 *Plasma Phys. Control. Fusion* **66** 075018